Longitudinal dispersion and lateral circulation in the intertidal zone

David K. Ralston and Mark T. Stacey
Department of Civil and Environmental Engineering, University of California, Berkeley, California, USA

Received 18 January 2005; revised 1 April 2005; accepted 9 May 2005; published 21 July 2005.

[1] Field observations indicate that a tidal salinity front that is regenerated each lower low water is a prominent feature of intertidal zone flow during wet winter months. A strong longitudinal density gradient at the front influences flow dynamics through tidal straining and baroclinic forcing. During each inundation period the salinity gradient disperses as it advects across the intertidal zone. The average longitudinal dispersivity estimated from observations is about 10 m^2 s^{-1}. A three-dimensional numerical model yields comparable estimates of tidally averaged dispersivity for an idealized bathymetry with a subtidal channel and intertidal shoals. The instantaneous dispersivity through the tidal cycle depends on both vertical and lateral shear in along-channel velocity. Dispersion due to vertical shear is greatest during stratified ebbs and inversely depends on tidal forcing; dispersion due to lateral shear results from bathymetric variability between channel and shoal and increases with tidal amplitude. Similarly, the along-channel residual velocity is a combination of baroclinic and frictional processes. Frictional effects dominate the depth-averaged residual such that net flow is upstream on the shoals and downstream in the channel; however, the frictional pattern is moderated by baroclinic forcing at the front. Although along-channel dynamics dominate, differential advection of the salinity front establishes lateral baroclinic circulation between channel and shoals. Lateral residual circulation is flood dominant with dense water moving out of channel near the bed and convergence from the shoals at the surface. At times near the front the lateral salt flux can significantly affect the salinity budget in the channel.

Citation: Ralston, D. K., and M. T. Stacey (2005), Longitudinal dispersion and lateral circulation in the intertidal zone, *J. Geophys. Res.*, *110*, C07015, doi:10.1029/2005JC002888.

1. Introduction

[2] Because estuaries are the intersection of marine and riverine environments, processes that mix water from the two sources fundamentally impact how the systems function. Salt is transported upstream from the coastal ocean by baroclinic circulation and dispersive mechanisms, and this salt flux is balanced by net outflow due to river input. The flux balance in an estuary sets the length of the salt intrusion and correspondingly the longitudinal salinity gradient. Fluxes of other scalars like sediment, phytoplankton, or larvae are similarly governed by advective and dispersive processes. However, salt flux is paramount to estuarine physics because the density gradient between fresh and salty water contributes to flow dynamics.

[3] The transport of salt upstream into an estuary occurs by several processes that collectively represent dispersive fluxes. Tidal motions and baroclinic exchange flow move salt down gradient into the estuary and may be characterized with a Fickian diffusion coefficient, K_x. The relative importance of the each dispersive process depends on conditions in the estuary: stratification, tidal forcing, and bathymetry. The strength of dispersive processes can vary over tidal timescales (e.g., diurnal [*Stacey et al.*, 2001], spring/neap [*Bowen and Geyer*, 2003]) and seasonal timescales (e.g., with river flow [*MacCready*, 1999; *Monismith et al.*, 2002]). The temporal variability in the longitudinal dispersivity (K_x) in an estuary depends on which dispersal mechanisms are most important in that system.

[4] Many researchers have noted the contribution of baroclinic circulation to upstream transport of salt. *Hansen and Rattray* [1965] solved analytically for baroclinic salt transport and associated K_x. Their similarity solution balanced baroclinic forcing due to the longitudinal salinity gradient ($\partial S/\partial x$) against the barotropic pressure gradient due to water surface slope and found that tidally averaged baroclinic salt flux is proportional to $(\partial S/\partial x)^3$. Baroclinic circulation is modulated by tidal mixing through the vertical eddy viscosity, as weaker mixing permits greater stratification and greater exchange flow [*Geyer et al.*, 2000]. The combination of weaker mixing and stronger stratification during neap tides can generate significant pulses of salt flux over relatively brief periods [*Bowen and Geyer*, 2003].

[5] Shorter timescale variability in stratification can also alter the salt flux. Tidal straining creates asymmetries in stratification between ebbs and floods [*Simpson et al.*, 1990]. During ebbs the buoyancy flux due to straining of $\partial S/\partial x$ is stabilizing, enhancing stratification and increasing vertical shear in along-channel velocity. During floods the

0148-0227/05/2005JC002888$09.00

advective buoyancy flux is destabilizing, mixing stratification and reducing velocity shear [*Burchard and Baumert*, 1998]. Ebb/flood asymmetries in velocity profile generate residual velocities and salt transport that can be related to the longitudinal salinity gradient through a horizontal Richardson number Ri_x [*Stacey et al.*, 2001]. Salt flux due to tidal straining also depends on tidal forcing, with greater transport during weak tides and strong stratification. Tidal asymmetry is the source of this dispersion, so it is difficult to assess these fluxes with long-term tidal averages.

[6] In addition to baroclinic salt flux, tidal pumping and trapping processes contribute to net transport through correlations in velocity and salinity. Depth variation across estuaries creates shear in along-channel velocity, and repeated over many tidal cycles, this leads to transverse structure in along channel residuals. In some estuaries tidal pumping due to transverse shear can be much greater than the baroclinic flux [*Fischer*, 1972]. Transverse gradients in along-channel velocity can also produce tidal trapping. Lower velocity water in side embayments or on shoals can be out of phase with the deeper channel, turning to ebb while the channel continues to flood and releasing trapped high-salinity water slowly back to the main channel. This phased exchange of salt across bathymetric relief enhances the net longitudinal dispersion [*Okubo*, 1973].

[7] Longitudinal dispersion due to lateral shear depends in part on the timescale of cross-sectional mixing, with maximum dispersion when the mixing timescale is approximately equal to the tidal period [*Fischer et al.*, 1979]. However, cross-sectional mixing depends on lateral shear in along-channel velocity through transverse baroclinic circulation. Differential advection during floods carries higher salinity water farther up channels than shoals, establishing transverse density gradients. Dense channel water flows out onto the shoals near the bed and shoal water converges at the channel surface. Mixing associated with lateral circulation tends to reduce lateral shear and associated longitudinal dispersion [*Smith*, 1976]. In the Conwy Estuary, differential advection of the longitudinal salinity gradient creates axial convergence at the surface during floods [*Nunes and Simpson*, 1985]; the strongest lateral circulation coincides with the maximum $\partial S/\partial x$ [*Turrell et al.*, 1996]. Alternatively in very wide estuaries where the timescale for mixing is much longer than one tidal period, transverse circulation may enhance exchange between channel and shoals and increase longitudinal dispersion [*Dronkers*, 1996].

[8] For most real estuaries the mechanisms behind longitudinal dispersion of salt present an unsteady, three-dimensional (3-D) problem linked to the flow dynamics, stratification, and bathymetry. Though natural variability makes generalizations difficult, we present here an environment that is representative of a broad class, intertidal zone mudflats and salt marshes at the edges of many coastal and estuarine systems. Flow dynamics and transport processes in the intertidal zone are in many ways similar to larger, deeper estuaries, but with forcing modified by the shallow depths. Tidal velocities over mudflats and marshes are relatively low magnitude for much of the tidal cycle, but as we will see the spatial density gradients can be seasonally very large. By applying traditional estuarine analyses to the intertidal zone we quantify fluxes into and out of these regions to better understand their functioning.

2. Background and Site Description

[9] These results are based on a series of field experiments in the intertidal zone of central San Francisco Bay. The study location is a mudflat and salt marsh area at the University of California's Richmond Field Station (Figure 1a). To characterize the spatial variability across the site, the field experiments measured near-bed velocity and scalar concentrations at multiple locations on the mudflat and in the subtidal channels passing through the mudflat and marsh. To cover the seasonal variability of the San Francisco Bay area, we collected data both during relatively dry summer and wet winter conditions. The results presented here focus on conditions through the wet winter months, when precipitation generates the freshwater runoff to the marsh. The large salinity difference between relatively fresh water upstream in the marsh ($\sim$5 psu) and much saltier conditions downstream in San Francisco Bay (>25 psu) across the relatively small width of intertidal zone creates a strong longitudinal density gradient. Though there are short-term modulations after large precipitation events, the strong density gradient persists throughout the winter months and is not just a transient response to individual storms.

[10] The wet season field experiments were two studies, one from 25 February to 2 March 2003 and one from 19 December 2003 to 3 January 2004. Results from the brief February 2003 experiment (discussed in greater detail by *Ralston and Stacey* [2005]) prompted the longer deployment in December 2003. To review the earlier work, we observed very strong periodic stratification in very shallow flow depths, particularly in the subtidal channels on the mudflats. Analysis of the turbulent shear stresses indicated that stratification significantly suppressed turbulent motions at times, while at other times in the tidal cycle turbulence was active and uninhibited by stratification. Strong stratification developed during ebbs because of tidal straining of the longitudinal density gradient, while tidal straining of $\partial S/\partial x$ during floods was destabilizing and reduced stratification.

[11] The strong $\partial S/\partial x$ coincides with a sharp front between salty bay water and fresher marsh water that each tidal cycle moves across the mudflats and marsh then back out to the bay. Because of the intertidal elevation, the front regenerates each time the mudflats are exposed around lower low water. Consequently, the system approaches a tidally periodic steady state in which the flow dynamics are influenced by periodic stratification and baroclinic forcing associated with the density gradient. This paper considers the salinity front as it advects and disperses through the intertidal zone, and specifically how the front affects flows and scalar transport in the system.

[12] Data from the December 2003 experiment corroborate the initial results from February 2003. The December experiment deployed sawhorse instrument frames at two locations along the axis of the subtidal channel, one on the mudflats (frame A) and one upstream in the marsh (frame B) (Figure 1b). On each frame instruments were mounted at several elevations near the bed: acoustic Doppler velocim-

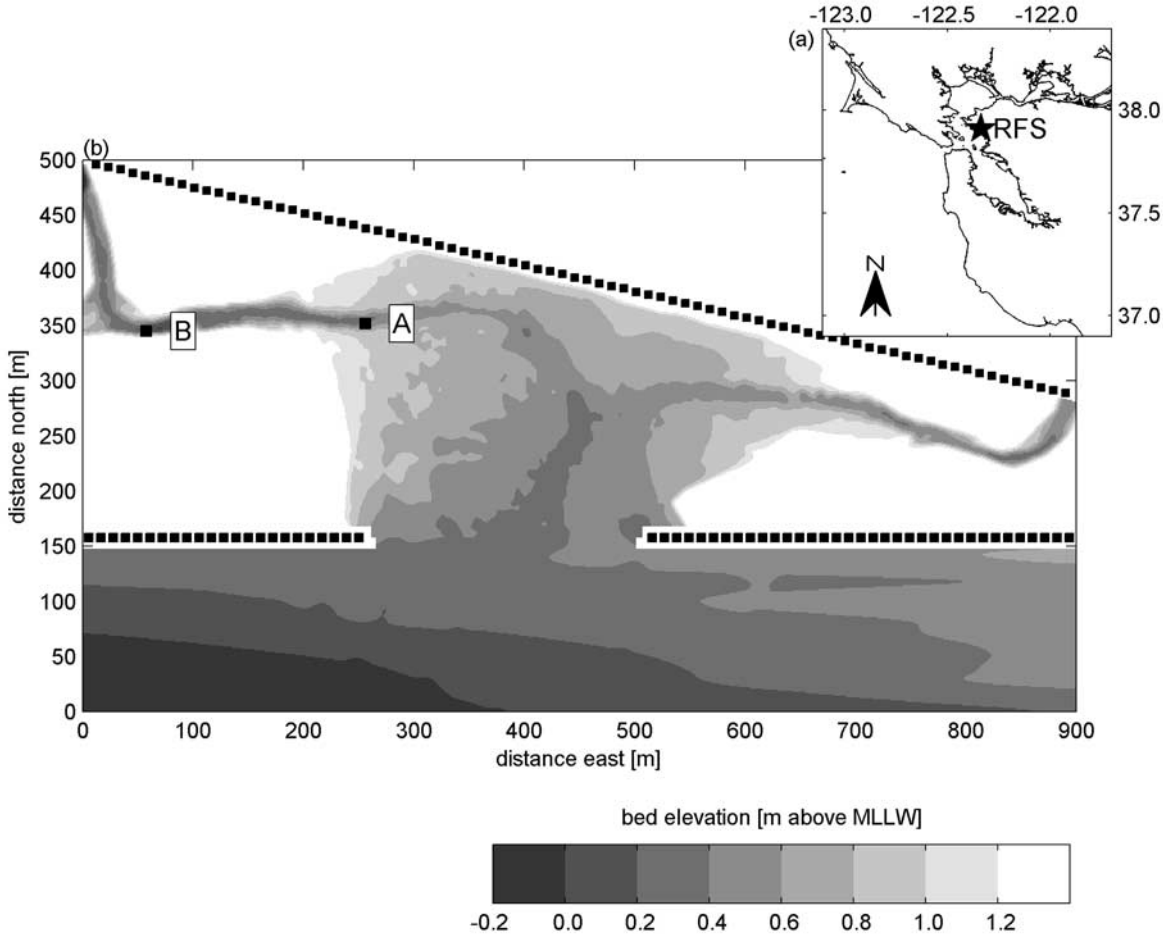

Figure 1. Location of field experiments. (a) Richmond Field Station (RFS) is on the eastern shore of central San Francisco Bay; and (b) bathymetry of the mudflats (shaded) and salt marsh (white). Instrument frames A and B were located in the subtidal channel flowing from the NW corner of the map out to San Francisco Bay at the southern edge of the map. Breakwaters protecting the southern edge of the salt marsh and a railroad berm across the northern edge of the mudflats are marked.

eters (ADVs), conductivity-temperature-depth sensors (CTDs), and optical backscatter sensors. On frame A (mudflat channel) the three ADV sample volumes were located 10, 25, and 40 cm above the bed, and CTDs sampled 10, 35, and 70 cm above the bed. On frame B (marsh channel) two ADVs were 25 and 40 cm above the bed and CTDs were 10 and 70 cm above the bed. The ADVs sampled at 16 Hz for 5 min bursts every 30 min. On frame A the two lower CTDs sampled every 30 s and the upper CTD sampled every 15 min. On frame B the lower CTD sampled every 7.5 min and the upper CTD every 15 min. The instruments collected data for 2 weeks, but 10 days into the experiment (29 December) a large precipitation event significantly increased flow in the channel and upset the instrument frames. We will limit our analysis to the period before the storm.

[13] During the December 2003 study tidal forcing was typical of San Francisco Bay, mixed semidiurnal with amplitude of about 2 m (Figure 2a). Several small precipitation events preceded the large storm of 29 December, but they did not significantly alter conditions (Figure 2b). Because the mudflat is south facing and protected on the other three sides by land or marsh, only winds from the south generate substantial wind waves at the study site. Periods of strong wind from the south are highlighted in the time series and have been removed from the analysis (Figures 2c and 2d).

[14] Water surface at the instruments mirrors offshore tidal forcing through most of the tide, but around lower low water when the mudflats are exposed water continues to flow down the subtidal channel at a relatively constant depth (Figure 2a). The inundation period between lower low waters is an important timescale for characterizing this system. A large fraction of the total volume of water in the system enters and exits each diurnal tidal period, so conditions are essentially reset and there is little memory of previous tidal cycles. Because of the diurnal inequality in tidal forcing, we divide the inundation period into an initial (strong) flood that wets the mudflat and marsh, a smaller (weak) ebb and a small (weak) flood that retain water on the flats, and finally a large (strong) ebb that exposes the intertidal zone.

[15] The salinity time series at frame A is indicative of variability on the tidal timescale, from less than 5 psu to

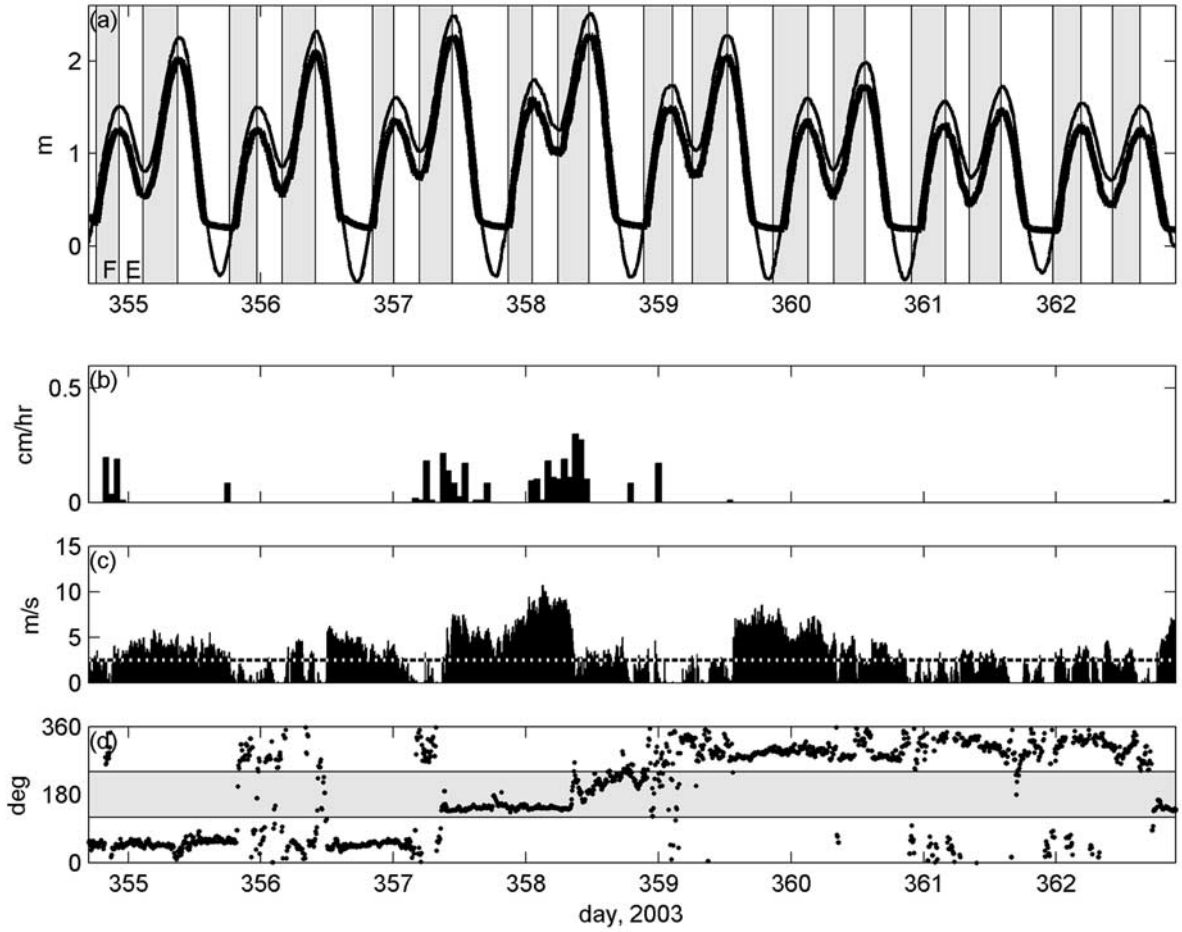

Figure 2. Tidal and meteorological conditions during the December 2003 deployment. (a) Tidal record from NOAA station at Richmond (thin line) and water surface elevation in the channel at frame A (thick line); (b) precipitation record during deployment; (c) wind speed during deployment, with reference line at 2.5 m s^{-1}; and (d) wind direction during deployment, with southerly winds highlighted. Because of the southern exposure of the mudflats, periods with strong winds from the south were removed from the analysis. Days 2–9 of the experiment are shown, leaving out the deployment on day 1 and major storm on day 10; these 8 days correspond with the salinity fronts in Figure 5.

more than 25 psu (Figure 3a). The upper bound is the salinity in central San Francisco Bay, while the lower values occur as the marsh drains around low water. Both water masses respond to precipitation, so there is some variability in the high and low salinities each tidal period. Additionally, variable tidal strength affects the transport of salt into marsh and thus salinity exiting at the end of the ebb. The salinity front appears in the time series as the very sharp rise in salinity at the start of each strong flood. During the strong ebb the decrease in salinity to fresher conditions is less rapid because of dispersion through the inundation period.

[16] With two instrument frames we measure the salinity gradient $\partial S/\partial x$ directly (Figure 3b). As the front passes the frames, the maximum $\partial S/\partial x$ are very large at about 50 psu km^{-1}. This is roughly 2 orders of magnitude greater than $\partial S/\partial x$ in central San Francisco Bay at the time. Upstream and downstream of the front $\partial S/\partial x$ drops substantially as the salinity is relatively constant. However, the strong density gradient over the narrow frontal region significantly alters the flow dynamics at the transition.

[17] One consequence of the strong salinity gradient is that tidal straining generates a large longitudinal buoyancy flux. Even though water depths are quite shallow and the measurements were near the bed, we observe periods of very strong stratification, salinity differences of 5 psu over 0.6 m and buoyancy frequencies ($N^2 = -g/\rho_0(\Delta\rho/\Delta z)$) of up to $\sim 10^{-1}$ s^{-2} (Figure 3c). Note that N^2 is calculated between fixed CTDs 10 and 35 cm above the bed. Stratification is variable on the tidal timescale, generally increasing during ebbs and decreasing during floods. At times during the floods we observe unstable salinity profiles near the bed with $N^2 < 0$. This is consistent with tidal straining advecting saltier water over fresher and forcing convective mixing. Through ebbs, stratification generally increases due to the stabilizing buoyancy flux. The exception is toward the end of strong ebbs when stratification breaks down and

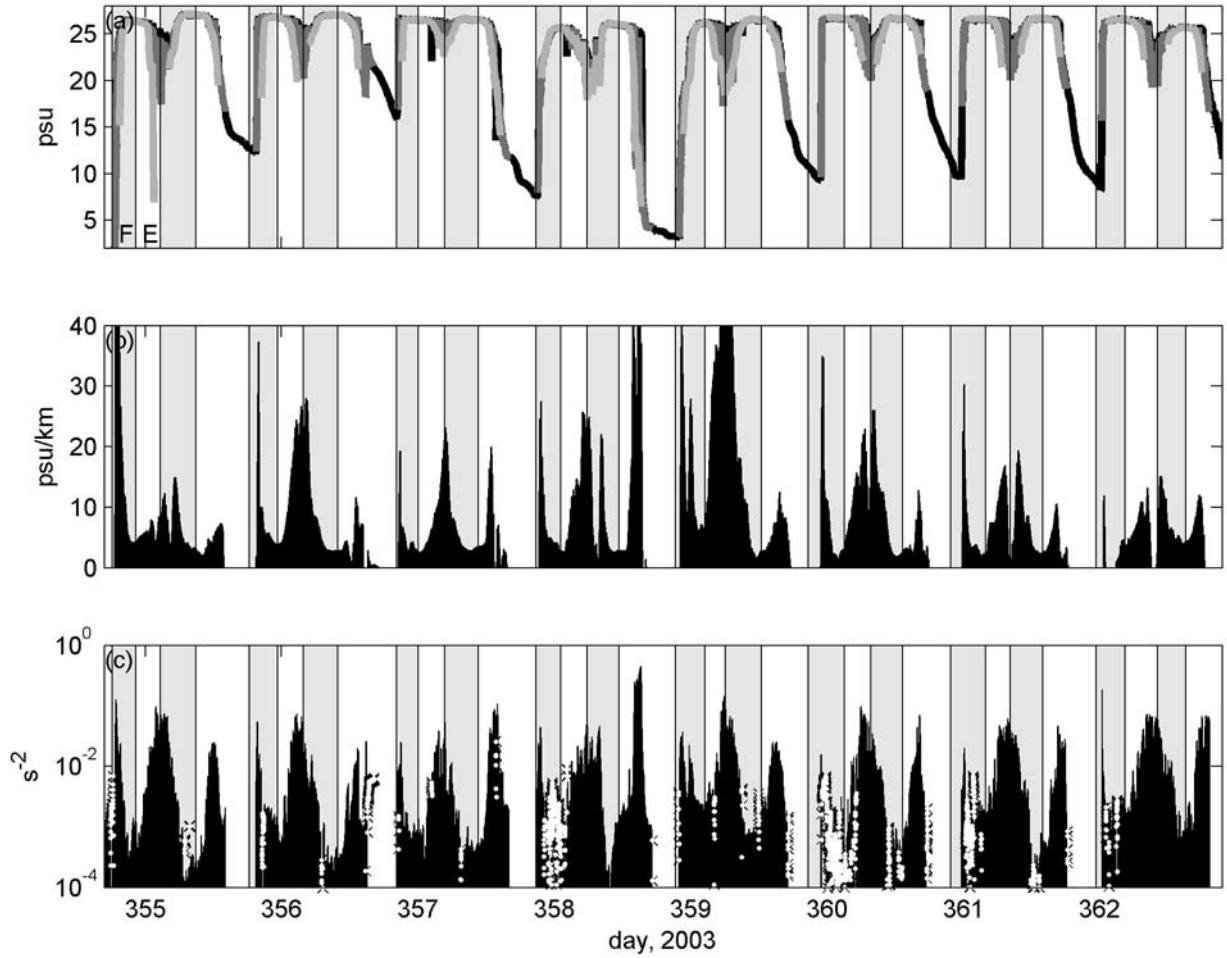

Figure 3. Salinity and stratification at frame A. (a) Salinity at three elevations in the channel, 10 cm (black), 35 cm (medium gray), and 70 cm (light gray) above the bed; (b) longitudinal salinity gradient ($\partial S/\partial x$) between frames A and B; and (c) stratification (N^2) at frame A measured between the bottom two salinity sensors. Negative N^2 (unstable stratification) are plotted with white dots, positive N^2 are in black.

N^2 decreases (e.g., $t \sim 357.6$ or 358.65). The combination of decreasing water depth and increasing velocity generates sufficient turbulence to exceed the buoyancy input and mix out stratification.

[18] Periodic stratification leads to ebb/flood asymmetries in the vertical mixing of momentum and scalars. During ebbs stratification suppresses turbulent mixing and the eddy viscosity decreases, while during floods mixing and the eddy viscosity are greater. Eddy viscosity is calculated from field measurements of Reynolds stress and shear: $\nu_t = -\overline{u'w'}(\partial U/\partial z)^{-1}$. When ν_t is scaled by depth-averaged velocity and water depth ($\nu_t = \alpha^* U^* H$), stronger mixing during floods appears as a larger scaling coefficient α (Figure 4a). If we assume a Prandtl number of about 1, the asymmetry also applies to vertical mixing of scalars.

[19] When mixing is suppressed during ebbs, lower eddy viscosity permits greater velocity shear. Additional shear enhances tidal straining of $\partial S/\partial x$, providing positive feedback that increases stratification. Tidal straining of $\partial S/\partial x$ during floods has the opposite effect on velocity shear as convective mixing homogenizes the water column and decreases shear. We see this asymmetry in velocity profiles between ebbs and floods in the field data, where for a given velocity shear is greater during stratified ebbs than during floods (Figure 4b). Together the asymmetries in stratification and velocity profile affect scalar fluxes and are important for longitudinal dispersion of the front.

3. Salinity Front Dispersion

[20] To better understand how the salt front evolves through the tidal cycle, we consider a simple model of one-dimensional advection and dispersion of the salinity gradient. The governing equation for depth-averaged salinity along the channel axis is then

$$\frac{\partial S}{\partial t} + U\frac{\partial S}{\partial x} = K_x \frac{\partial^2 S}{\partial x^2} \tag{1}$$

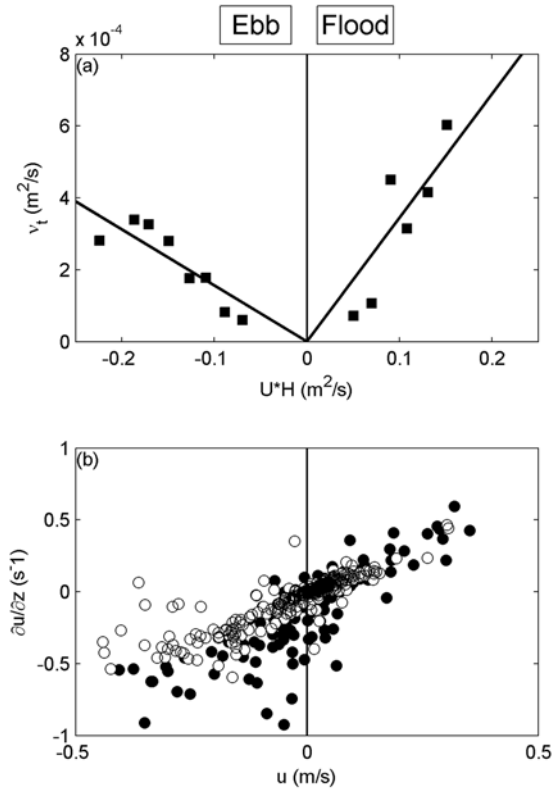

Figure 4. Asymmetries between flood and ebb conditions. (a) Eddy viscosity (ν_t) scaled by velocity times depth (U^*H) with best fit lines. The slopes of the lines are scaling coefficients (α), with larger α for more active mixing during floods. (b) Shear ($\partial u/\partial z$) plotted against velocity, with periods of stronger stratification ($N^2 > 5 \times 10^{-3}$ s^{-2}) as solid circles. During ebbs stratification leads to lower ν_t and greater shear than at corresponding velocities during floods.

where U is along-channel velocity and K_x is longitudinal dispersivity of salt. Idealizing the initial sharp gradient as a step function, we solve analytically for the salinity distribution through time advecting with the front at velocity U. The solution is

$$S(x,t) = \frac{S_0}{2}\left(1 + \mathrm{erf}\left(\frac{x - x_c}{\sqrt{4K_x t}}\right)\right) \quad (2)$$

where S_0 is the initial magnitude of the step function for $\partial S/\partial x$ and x_c is the center of the front that advects at the local velocity, or $x_c = \int_0^t U(t)dt$.

[21] To compare this 1-D model with field data, we calculate the width of the front as it passes each of the instrument frames through the tidal cycle. The distance between isohalines is the time-integrated velocity between isohalines advecting past the frames. In this way we convert salinity time series to spatial distributions assuming pure advection and get the salt field as a function of distance along the channel axis. To normalize several days of data, isohaline location is plotted with respect to distance to the middle of the front (S = 20 psu) (Figure 5). Salinity and velocity time series allow us to resolve much of the front at both frames during the strong flood and strong ebb periods, and at frame B during the intervening weak ebbs and floods.

[22] The snapshots of the salinity distribution through the tidal cycle show that dispersive processes widen the front and decrease the maximum $\partial S/\partial x$. We fit the 1-D analytical solution to the field data to get a rough estimate of the longitudinal dispersivity in the system and find $K_x \sim 10$ m^2 s^{-1} (Figure 5, dashed lines). Eight days of data are plotted, and while the analytical solution does not hold for all of the days it generally does a good job of tracking the spread of the front. The diurnal inundation period recreates the sharp front at low water so the pattern repeats each tidal cycle. Outlying salinity profiles result from changing meteorological conditions. Out on the mudflats frame A is exposed to wind more than frame B. Winds from the south during the strong ebbs of days 357 and 358 drove bay water up onto the flats and retarded the ebb as it exited of the marsh. This compressed the salinity front prior to its advection past frame A, decreasing the observed front width. In addition to wind, the analytical model does not adjust for changing boundary conditions. Both the bay water and marsh water are fresher after precipitation, changing the size of the initial gradient between the two water masses.

[23] A more fundamental limitation of the analytical model is that the dispersivity is not necessarily constant spatially across the front or temporally through the tidal cycle. The quality of the fit to the data varies across the front, with apparent dispersivity generally greater on the fresh side of the front. As a check we can compare the implied dispersivity of about 10 m^2 s^{-1} with standard scaling estimates of K_x. Assuming an unstratified water column, uniform channel cross section, and unidirectional logarithmic velocity profile, scaling predicts $K_x \sim 5.93 u_* H$, where u_* is the friction velocity and H is the water depth [*Fischer et al.*, 1979]. Such scaling that strongly depends on depth is ill defined in the intertidal zone where the tidal variability in water depth is greater than the mean depth, but we can assume nominal values of H $\sim$ 1 m and $u_* \sim 0.05 * U_{\mathrm{RMS}} = 0.05 * (0.1 \text{ m s}^{-1}) = 0.005$ m s^{-1}. The resulting estimate of K_x is 0.03 m^2 s^{-1}, 2–3 orders of magnitude lower than the field value. Apparently, this simple scaling does not account for all the dispersive processes in the intertidal environment.

[24] An alternative scaling might include tidal trapping due to phasing between the channel and higher elevation mudflat and marsh surfaces. *Okubo* [1973] developed scaling for tidal trapping based on the tidal period and the exchange time between the main channel and side embayments. For oscillatory main channel flow of $u = u_0 \cos(\sigma t)$ the effective longitudinal dispersivity is

$$K_x = \frac{K_{x0}}{1+r} + \frac{r u_0^2}{2k(1+r)^2(1+r+\sigma/k)} \quad (3)$$

where K_{x0} is the dispersivity in the main channel, r is the ratio of trap volume to channel volume, and k^{-1} is a characteristic exchange time between channel and traps. With this scaling we can check if tidal trapping is a plausible source of dispersion for the field estimate of $K_x \sim 10$ m^2 s^{-1}. Defining the trap zones as the mudflat and marsh shoals we estimate the width of these regions as 100 m. If the velocity scale for exchange between channel and shoal is about 2 cm s^{-1}, then $k \sim (0.02 \text{ m s}^{-1})(100 \text{ m})^{-1} \sim 2 \times 10^{-4}$ s^{-1}. Assuming $u_0 \sim 20$ cm s^{-1} and $\sigma \sim 1.4 \times 10^{-4}$ s^{-1}, then an

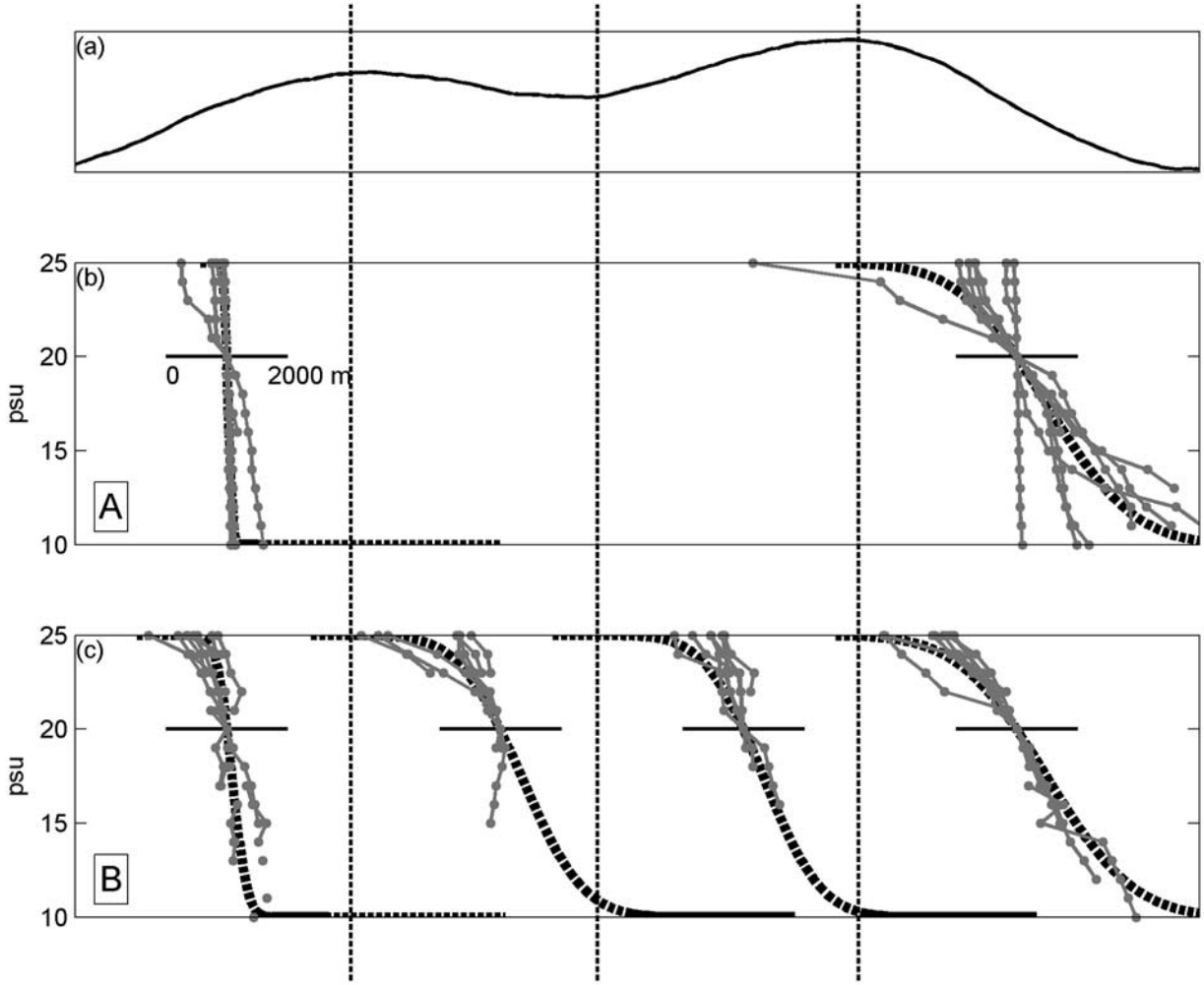

Figure 5. Salinity front at the instrument frames. (a) Schematic of water surface elevation through a typical diurnal tidal cycle; (b) spatial distribution of salinity field observed at frame A during strong flood and strong ebb; and (c) distribution of salinity field observed at frame B during strong flood, weak ebb, weak flood, and strong ebb. Salinity distributions are calculated from salinity and velocity time series at the frames assuming pure advection of the salinity field. The width of each salinity front (8 days) is plotted relative to the location of the 20 psu isohaline, and the dashed lines represent analytical dispersion with $K_x = 10\ m^2\ s^{-1}$. In each frame the horizontal bar represents 2000 m. During the weak ebb and weak flood the entire front region did not advect past frame A, so those periods are omitted.

effective K_x of 10 $m^2\ s^{-1}$ with this scaling would require the ratio of trap to main channel to be $r \sim 1$. This is not an unreasonable value for the simplified geometry we have described; for wide ($w \sim 100$ m), shallow ($h \sim 0.5$ m) shoals and a narrow ($w \sim 25$ m), deep ($h \sim 2$ m) channel the ratio is 2. Although a plausible value of r produces a tidal trapping dispersivity scale of the same order as the field data, it is not clear that the Okubo framework is appropriate in this environment. The tidal trapping mechanism is an integrated effect of multiple tidal cycles and is appropriately applied to tidally averaged flow and salinity. In contrast to fully subtidal estuaries, the intertidal zone does not offer meaningful tidal averages for this type of analysis. Because the tidal excursion length is much greater than the length of the salt field (i.e., frontal region), the temporal deviation of salinity at a point from the tidal average is the same magnitude as the tidal average. The phasing and exchange between channel and shoals may yet be important to the evolution of the salt front through the tide, but the interaction of tidal current shears with small-scale mixing within a tidal cycle must be the primary consideration. Unfortunately, the field data do not permit a complete evaluation of the lateral and vertical shears in the system, so we turn to a numerical model for the remainder of this analysis.

4. Numerical Model

[25] The tidal, residual, intertidal mudflat (TRIM) model is a three-dimensional finite difference code for flow and scalar transport [*Casulli and Cattani*, 1994; *Gross et al.*, 1998]. TRIM solves the Reynolds-averaged Navier-Stokes

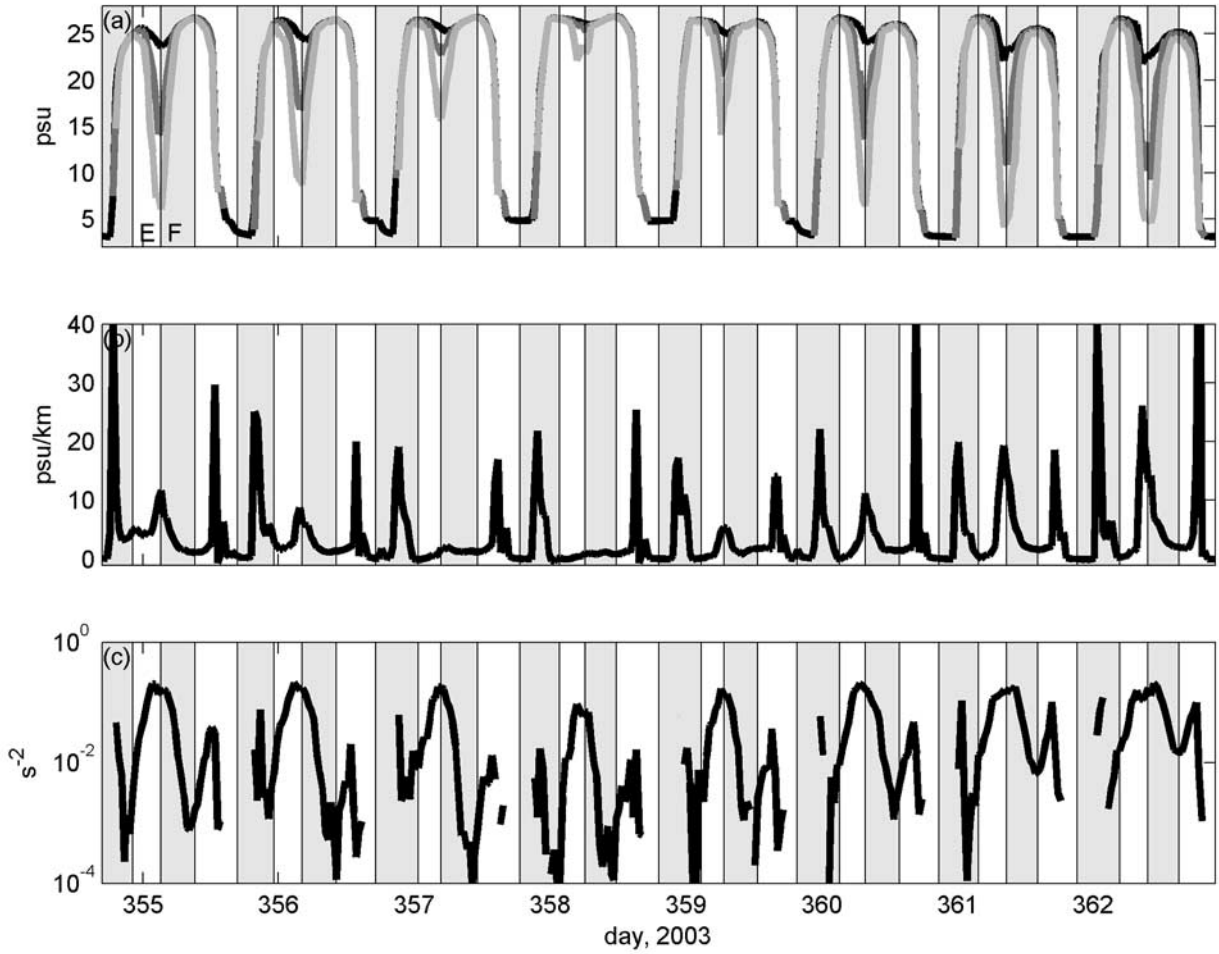

Figure 6. Numerical model results using tidal forcing during the December 2003 field deployment and sampled from the subtidal channel for comparison with observations. (a) Salinity at three elevations in the channel, 10 cm (black), 35 cm (medium gray), and 70 cm (light gray) above the bed; (b) longitudinal salinity gradient ($\partial S/\partial x$) at sample location; and (c) stratification (N^2) at elevation of salinity sensors. The numerical results compare favorably with the field data (Figure 3), especially given the simplified model bathymetry. The sample location corresponds with the transverse profile in Figures 7 and 8.

equations, parameterizing turbulence with Mellor-Yamada level 2.5 closure [*Galperin et al.*, 1988]. An important feature for this intertidal application is that the model efficiently handles wetting and drying of cells. The grid for the model is a vastly simplified version of the field site, a straight subtidal channel with intertidal flats on either side. The domain has a constant slope of 0.0005, a value consistent with the bathymetry at the field site. The grid spacing is 15 m horizontally and 0.1 m vertically. At the closed upstream end of the channel is a reservoir of relatively fresh water at 5 psu, and at the downstream end is an open boundary condition at bay salinity of 28 psu. Because most of the domain drains with each diurnal tidal cycle, the model requires only a very brief spin-up time to reach a periodic steady state.

[26] To compare numerical results with the field observations, we used a NOAA station record during the December 2003 deployment to force the water surface elevation at the open boundary. Despite the simplified domain, the model does a good job of reproducing the features we see in the field. We extract results from a point in the channel midway up the intertidal zone for comparison with the instrument measurements (Figure 3). The salinity time series captures the tidal variability between bay and marsh conditions (Figure 6a). Near the front $\partial S/\partial x$ is quite large, but elsewhere the gradient drops to much lower values (Figure 6b). The maximum magnitude of $\partial S/\partial x$ in the model is slightly lower than the maximum observed in the field, perhaps because precipitation that intermittently strengthened $\partial S/\partial x$ is not incorporated in the model. Stratification in the channel follows the tidal periodicity observed in the field, generally increasing through ebbs and decreasing through floods (Figure 6c). The model also reproduces exceptions to this pattern, including the breakdown of stratification at the end of the ebb and the relatively large N^2 midway through the strong flood. Con-

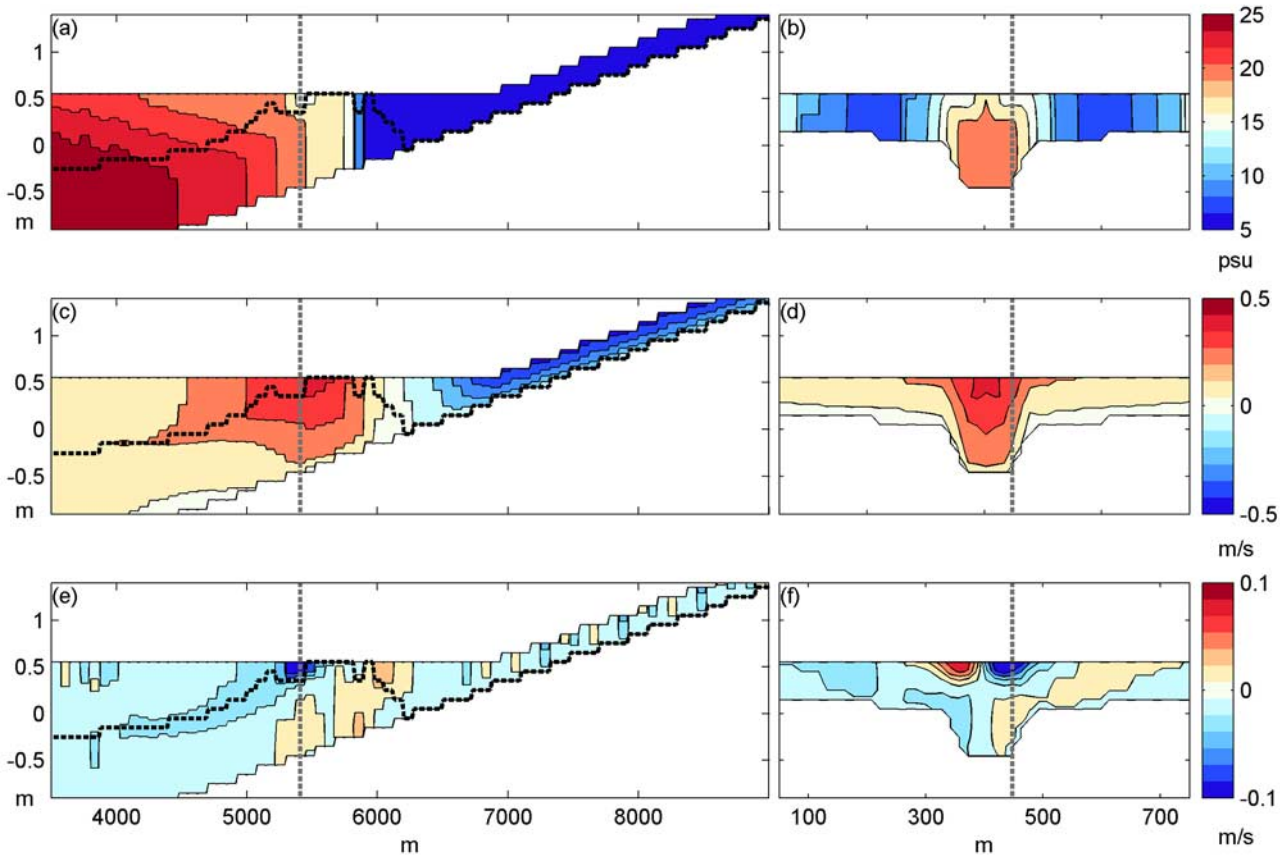

Figure 7. Longitudinal and transverse profiles of numerical model results during a flood tide. (a–b) Salinity; (c–d) along-channel velocity (u, flood > 0); and (e–f) across-channel velocity (v). The location of the longitudinal profiles is shown in the transverse profiles (gray dashed line) and vice versa; longitudinal profiles are offset from the channel center to show the lateral circulation. The elevation of the maximum along-channel velocity is plotted in the longitudinal profiles (black line).

sequently, we are relatively confident that the numerical model incorporates the dominant physical processes at the field site.

[27] The numerical model offers a more complete picture of the front evolution than was available from the observations. We plot salinity, along-channel velocity, and across-channel velocity at representative times during flood and ebb. The longitudinal structure is shown in profiles along the channel and the transverse structure is shown with cross sections at the sample location for the time series in Figure 6. As the salinity front moves up the channel during the flood, isohalines are compact and nearly vertical (Figure 7a). Velocity is stronger in the channel than on the shoals (Figure 7d), and differential advection carries saltier water farther up the channel to establish a transverse density gradient (Figure 7b). Transverse baroclinic circulation is strongest immediately behind the salinity front, advecting dense water out of the channel near the bed and returning fresher, lower momentum water from the shoals to the surface of the channel (Figures 7e and 7f). The transverse baroclinic circulation alters the structure of the water column immediately behind the front, creating strong stratification (Figure 7a) and a subsurface maximum in along-channel velocity (Figure 7c).

[28] Because of the asymmetry in tidal straining, the salinity front structure during ebbs is very different than during floods. Midway through the ebb, isohalines are nearly horizontal and the frontal zone has elongated (Figure 8a); the entire cross section is strongly stratified (Figure 8b). The maximum along-channel velocity during ebbs is near the surface, and the velocity profile is strongly sheared throughout (Figures 8c and 8d). Although along-channel velocity is greater in the channel than on the shoals, there is little transverse density gradient (Figure 8b). Without transverse density gradients the lateral circulation reflects spreading of a buoyant plume (Figures 8e and 8f). This snapshot is representative of conditions during most of the ebb, and transverse baroclinic structure due to fresher water in the channel does not develop until stratification breaks down near the end of the ebb.

5. Along-Channel Residual Velocities

[29] Upstream salt flux is in part driven by steady residual velocities into and out of the estuary. Horizontal density gradients create baroclinic residual flow of dense inflow near the bed and fresher outflow near the surface. However, bathymetric variability can also create residuals such that

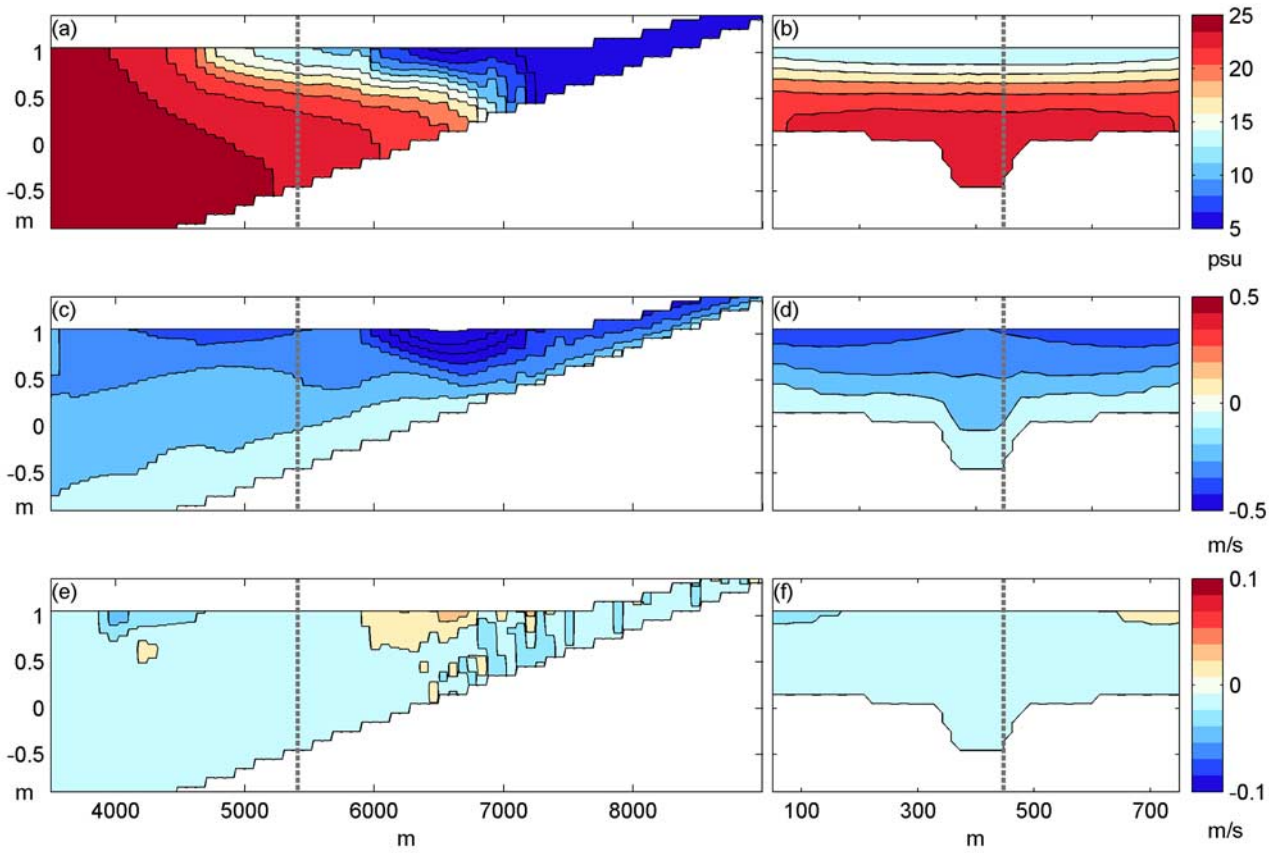

Figure 8. Longitudinal and transverse profiles of numerical model results during an ebb tide. (a–b) Salinity; (c–d) along-channel velocity (u, flood > 0); and (e–f) across-channel velocity (v). The location of the longitudinal profiles is shown in the transverse profiles (gray dashed line) and vice versa; longitudinal profiles are offset from the channel center to show the lateral circulation.

the combination of baroclinic and bathymetric effects sets the total residual flux. Considering only baroclinic forcing, bathymetric relief shifts dense inflow to deeper channels and fresher outflow to shallow shoals [*Wong*, 1994]. Frictional effects have the opposite pattern with depth. Because of the nonlinearity of bottom friction and tidal wave propagation, a frictional system without density gradients has flood dominant shoals and return flow out the channel [*Li and O'Donnell*, 1997]. Tidal asymmetry can also impact residual flow; for a partially progressive wave, intertidal shoals are inundated for more of the flood than the ebb, enhancing the frictional pattern of flood dominant shoals [*Bowers and Al-Barakati*, 1997]. Cases with both frictional and baroclinic forcing will reflect a balance between the two factors. For example, a comparison of the mechanisms in the James River found that the balance depended on tidal forcing, with the baroclinic residual dominating during more stratified neap tides [*Li et al.*, 1998].

[30] Baroclinic forcing is strongest near the salt front where $\partial S/\partial x$ is largest. Most standard approaches to calculating the strength of baroclinic circulation tidally average conditions and assume that $\partial S/\partial x$ is nearly constant through the estuary. Tidally averaged approaches like the *Hansen and Rattray* [1965] classification or the estuarine Richardson number [*Fischer*, 1972] balance the strength of the longitudinal density gradient against turbulent mixing. Applying either approach to the field data, we find that the large magnitude $\partial S/\partial x$ near the front coupled with relatively low tidal velocities should generate highly stratified conditions and strong baroclinic circulation. However, away from the salt front the baroclinic forcing drops substantially and the estuarine classification shifts toward more well-mixed character. Although tidally averaged characterizations can be useful, they are particularly ill suited to the intertidal zone. Defining meaningful averages for parameters is problematic when $\partial S/\partial x$, water depth, and estuarine width vary over orders of magnitude both spatially and temporally. Additionally, tidally averaged approaches do not capture salt transport due to asymmetries between ebbs and floods [*Stacey et al.*, 2001]. The tidal timescale is most relevant in the intertidal zone because the diurnal inundation makes processes over longer timescales less important for mean flows.

[31] In this system, the residual velocity does represent a balance between the baroclinic and frictional patterns (Figure 9). The residual at each cross section is simply a temporal average of the velocity in each cell. The cross-sectional average velocity due to freshwater is removed before calculating the along-channel residual: $u_R = Q_R/A$, where Q_R is the river flow and A is the local cross-sectional flow area. On the shoals the vertical profile of the along-channel residual has the classic baroclinic pattern, upstream

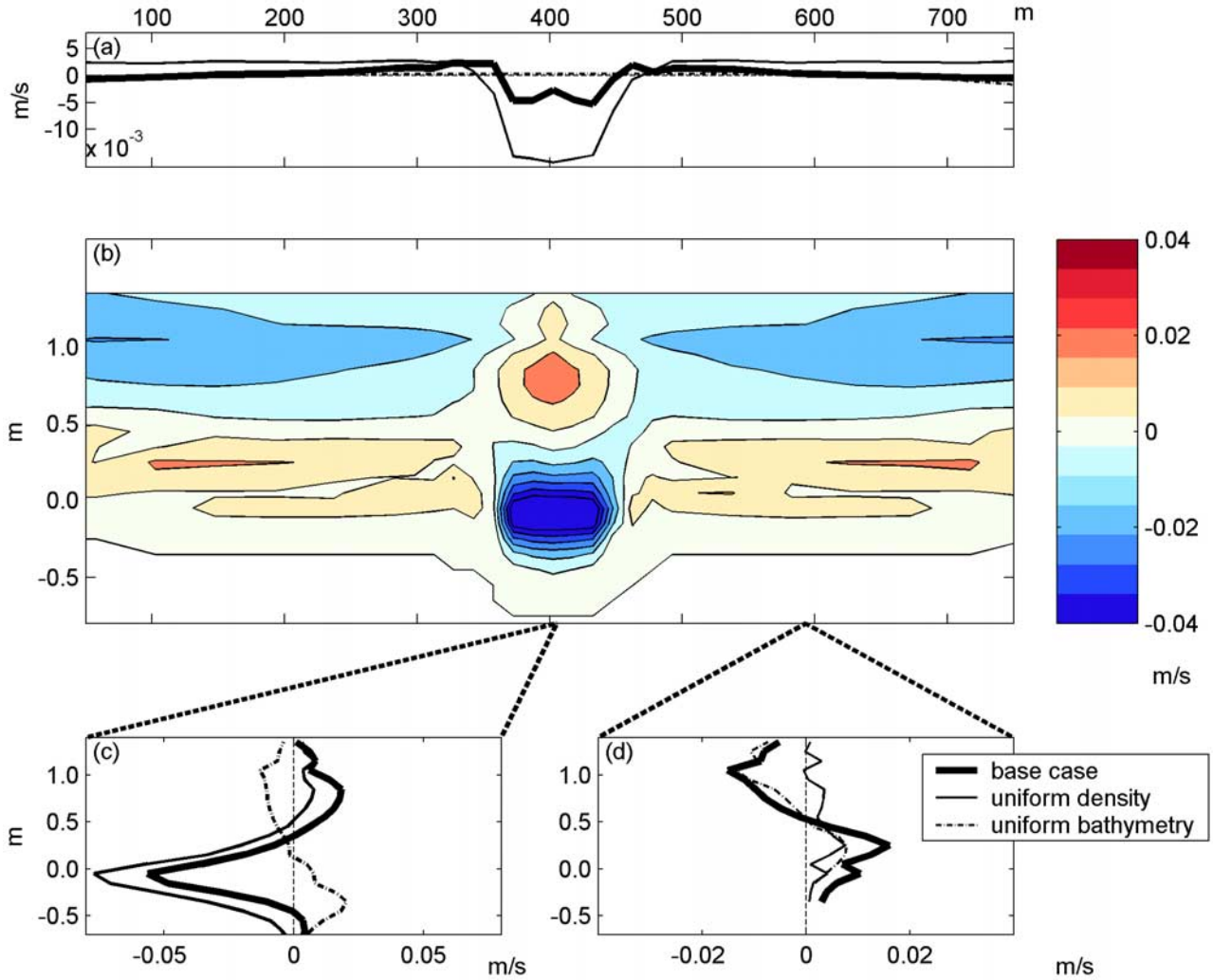

Figure 9. Longitudinal residual velocity from numerical model. (a) Depth average of longitudinal residual (flood > 0); (b) cross section of longitudinal residual; (c) vertical profile of longitudinal residual in channel; and (d) vertical profile of longitudinal residual on shoals. In Figures 9a, 9c, and 9d the thick solid line is the base case, the thin solid line is a case with uniform density (no baroclinic effects on residual), and the thin dashed line is a case with uniform bathymetry of a flat bottom and no channel (no bathymetric effects on residual).

near the bed and downstream at the surface (Figure 9b). In the channel the residual profile switches to a frictional structure, downstream near the bed and upstream near the surface. Because of the shallow environment and large relative change in depth between channel and shoal, the depth average of along-channel residual is predominantly frictional (Figure 9a, thick line). Net flow is upstream on the shoals and back out to the bay in the channel. However, the strong baroclinic forcing at the salinity front does alter the pattern from a purely frictional case. In the deepest part of the channel baroclinic forcing is stronger than on the channel banks, and consequently residual flow in the channel center ($x \sim 400$ m) is less strongly downstream than on the banks ($x \sim 375$ and 425 m).

[32] We can directly assess the effect of the density gradient on residual circulation through equivalent numerical model runs with uniform density. In the uniform density case the depth average residual is strictly frictional, with much stronger residual flow downstream in the channel and flow upstream on the shoals (Figure 9a, thin solid line). In the base case the baroclinic circulation opposes the frictional residual to limit the net flow out of the channel. Similarly, we can experiment numerically to see the role of bathymetry by removing the channel from the model grid. Without the depth variation and focusing toward the channel during ebbs, the residual longitudinal pattern has a purely baroclinic structure across the domain; depth-averaged circulation is nearly uniform and zero (Figure 9a, thin dashed line). The vertical structure of the residual also reflects the balance between the bathymetric and baroclinic factors. In the channel the uniform density case is downstream near the bed and upstream near the surface (Figure 9c, thin solid), while the uniform bathymetry case has the opposite form, upstream at the bed and downstream at the surface (Figure 9c, thin dashed). The base case falls between the two, but is closer to frictional, uniform density

Table 1. Longitudinal Dispersivity Versus Tidal Amplitude

η, m	K_X^V, m^2 s^{-1}	K_X^T, m^2 s^{-1}	$K_X = K_X^V + K_X^T$, m^2 s^{-1}
0.50	22	2	24
0.75	15	15	30
1.00	10	37	47
1.00/0.50	16	19	35

case (Figure 9c, thick solid). On the shoals the base case (Figure 9d, thick solid) closely resembles the baroclinic pattern of the uniform bathymetry case (Figure 9d, thin dashed). The vertical profile of the residual in the uniform density case is predominantly upstream on the shoals (Figure 9d, thin solid) to balance the downstream flow in the channel.

6. Salt Fluxes

[33] We are interested in how asymmetries in stratification, velocity shear, and transverse circulation influence dispersion of the salinity gradient through the inundation period. The salt flux through a section across the model domain can be decomposed into spatial variations to define mechanisms generating dispersive fluxes. Other estuarine analyses follow a similar flux decomposition approach, but flux components are typically tidally averaged to calculate long-term dispersion coefficients [e.g., *Fischer*, 1972]. However, we are interested in how the dispersive mechanisms vary within a tidal cycle. Rather than the weekly to monthly adjustment timescale for larger estuaries [*MacCready*, 1999], the dominant timescale for the intertidal zone is the diurnal inundation period. Therefore the following flux decomposition is only spatial, solving for instantaneous salt fluxes and associated instantaneous longitudinal dispersivities.

6.1. Longitudinal Flux Decomposition

[34] To begin the spatial decomposition, the instantaneous velocity and salinity are written as cross-sectional averages plus deviations from those averages. The deviations can then be further decomposed into transverse and vertical structures. The quantities remaining after removal of the cross-sectional means are averaged across the width of the domain and the decomposition becomes

$$\begin{aligned} u(x,y,z,t) &= u_A(x,t) + u_V(x,z,t) + u_T(x,y,z,t) \\ s(x,y,z,t) &= s_A(x,t) + s_V(x,z,t) + s_T(x,y,z,t) \end{aligned} \tag{4}$$

where u and s are the instantaneous values. The subscript A indicates cross-sectional averages that vary along the channel axis (x), and subscripts V and T represent remaining vertical (z) and transverse (y) structures, respectively.

[35] Because the variation in depth in this environment is large with respect to the mean depth, correlations among velocity, salinity, and cross-sectional area are important for net fluxes in the system. We account for changes in flow area by writing in the instantaneous salt budget as

$$\frac{\partial}{\partial t}(As_A) + \frac{\partial}{\partial x}(Au_A s_A) = \frac{\partial}{\partial x}\left(A\left(K_x^V + K_x^T\right)\frac{\partial s_A}{\partial x}\right) \tag{5}$$

where u_A and s_A are cross-sectional averages and the remaining flux terms are expressed as dispersive fluxes. Longitudinal dispersion is subdivided such that K_x^V is the dispersivity due to vertical structure in velocity and salinity and K_x^T is the dispersivity due to transverse structure. Dispersivities are calculated from the decomposed correlations of velocity and salinity with the depth-averaged salinity gradient. From the decomposition, the instantaneous dispersivities are

$$\begin{aligned} K_x^V &= -\langle u_V s_V \rangle_A \left(\frac{\partial s_A}{\partial x}\right)^{-1} = \frac{\int_0^H W(z) u_V s_V dz}{A}\left(\frac{\partial s_A}{\partial x}\right)^{-1} \\ K_x^T &= -\langle u_T s_T \rangle_A \left(\frac{\partial s_A}{\partial x}\right)^{-1} = \frac{\int_0^W \int_0^H u_T s_T dz dy}{A}\left(\frac{\partial s_A}{\partial x}\right)^{-1} \end{aligned} \tag{6}$$

where $\langle u_V s_V \rangle_A$ and $\langle u_T s_T \rangle_A$ are cross-sectional averages of the vertical and transverse structure fluxes, W is the width, and H is the depth. Using local fluxes and salinity gradients, we calculate dispersivities throughout the model domain. Again, these are instantaneous dispersivities that vary both temporally and spatially.

[36] The model open boundary condition is a sinusoidal water surface with a 12 hour period and fixed amplitude. Instantaneous dispersivities vary greatly through the tidal cycle so we initially summarize the results by calculating an average dispersivity for the system. We define this bulk dispersivity by averaging instantaneous dispersivities through the tidal period and over length of the salinity front intrusion. This bulk dispersivity is useful for comparing changes with tidal forcing; how the tidal forcing impacts the instantaneous dispersivities will be discussed in greater detail later. We start with an amplitude of 0.75 m, a tidal range that falls between the strong and weak forcing of the field deployment. For 0.75 m tides the bulk dispersivity due to vertical correlations in the salt flux is about 15 m^2 s^{-1}, while the dispersivity due to transverse structure is also about 15 m^2 s^{-1}. The total dispersivity then is about 30 m^2 s^{-1}, roughly consistent with the 1-D analysis of the field data that estimated $K_x \sim 10$ m^2 s^{-1}.

[37] Vertical shear dispersivity depends on stratification and transverse shear dispersivity depends on differential advection between channel and shoal, so both are linked to the strength of the tidal forcing but with opposite sense. Stronger tidal forcing generates turbulence that mixes away stratification, so K_x^V decreases with stronger tides. On the other hand, higher velocities and nonlinear frictional response generate greater differential advection between shallow and deep regions so that K_x^T increases with stronger tides. These trends are consistent with the results of varying the amplitude of the boundary forcing (Table 1). For 0.5 m amplitude tides, stratification effects dominate dispersion and K_x^V is much greater than K_x^T. For 1.0 m tides, bathymetric effects are more pronounced as K_x^T is greater than K_x^V. For the 0.75 m tides the mechanisms have similar contributions to the total dispersivity.

[38] Variability with tidal amplitude is important on both diurnal and spring/neap timescales. We idealize the diurnal inequality in field data with mixed amplitude forcing at the boundary (Figure 10a). The bulk vertical and transverse dispersivities in the mixed tide case are similar to the 0.75 m

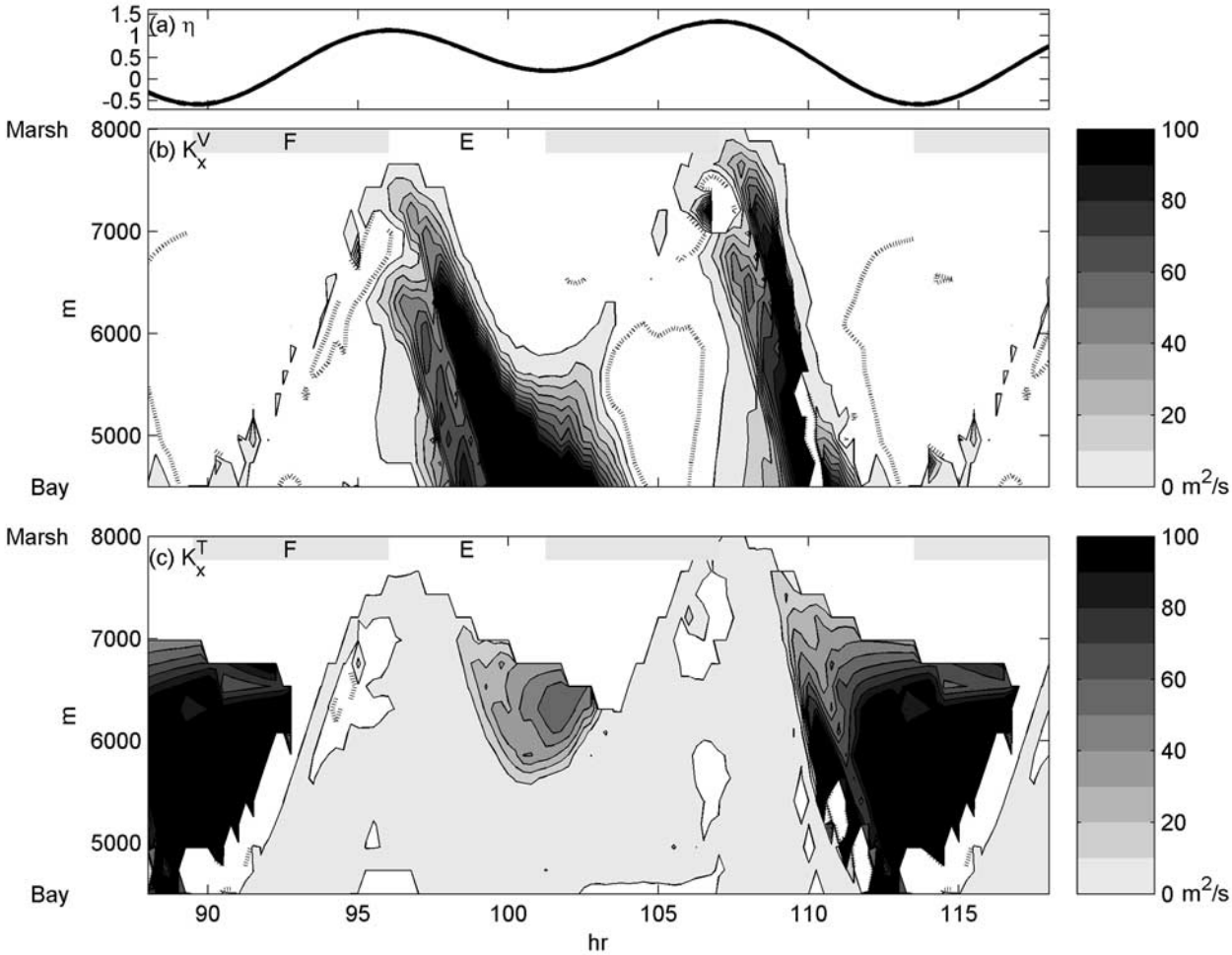

Figure 10. Instantaneous longitudinal dispersivities (K_x) from numerical model. (a) Water surface at boundary (x = 0 m) with semidiurnal inequality; (b) dispersivity due to vertical structure in shear and salinity (K_x^V); and (c) dispersivity due to transverse structure in salt flux (K_x^T). Dashed lines are negative contours (-10 m^2 s^{-1}). The tidal open boundary condition (bay) is toward the bottom of the figure and the closed boundary (marsh) is toward the top.

tidal forcing (Table 1). However, K_x^V and K_x^T are not at all constant through the tidal cycle, and the mixed diurnal tidal forcing is illustrative of the temporal variability. Instantaneous dispersivities along the channel axis are contoured for a diurnal period, separating the K_x^V and K_x^T components (Figures 10b and 10c). In these plots the tidal open boundary condition is toward the bottom of the figure and the closed marsh boundary is toward the top; time is the abscissa. Tidal oscillation of the frontal zone from the bay up the channel toward the marsh corresponds with the region of nonzero dispersivities; away from the front $\partial S/\partial x$, K_x^V, and K_x^T are all much lower.

[39] Examining the variability with the mixed diurnal tide, we note that the vertical structure is particularly strong during stratified ebbs when strained isohalines are advected downstream at the surface (Figure 10b). Stratification is present throughout the weak ebb ($t \sim 96$–102 hours), and vertical shear structure dominates the dispersion. During the strong ebbs turbulent mixing breaks down stratification midway through the tide ($t \sim 110$ hours), and the vertical structure of salt flux disappears. For the remainder of the strong ebb the water column has vertically homogenous salinity, and K_x^V remains relatively low for the rest of the tidal cycle.

[40] At times just after low water the K_x^V actually becomes negative, indicating salt flux up gradient ($t \sim 105$ hours, dashed contour). *Larsen* [1977] proposed that up-gradient fluxes are possible due to phasing between flow near the bed or walls and the central flow region, but negative dispersion should be confined to these near-wall regions. *Smith* [1982] showed that in oscillating flows negative dispersivities are possible at flow reversal as the scalar gradient is sharpened by the changing flow direction. One source of apparent negative dispersivity at flow reversal is an artifact of vertical averaging, but real negative dispersivities are possible in oscillatory flows during initial dispersion of a scalar gradient [*Yasuda*, 1984]. Negative dispersivities are possible in this case because dispersion in the system does not reach the stationary stage with the diurnal inundation period. Negative dispersivities are inconsistent with the Fickian dispersion model for salt flux, so incorporating this effect into tidally averaged analyses presents a challenge.

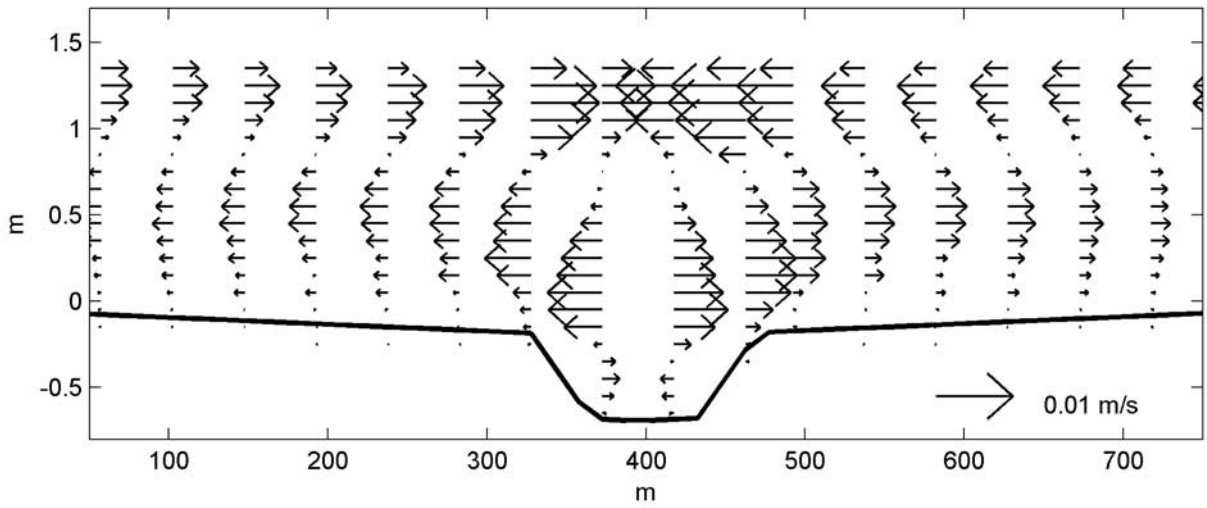

Figure 11. Lateral residual velocity from numerical model. Cross section location is same as in Figures 7, 8, and 9.

[41] Transverse shear dispersivity is also variable in space and time. The maximum K_x^T also occur during ebbs, but on the trailing edge of the front where the water column has destratified (Figure 10c, $t \sim 110-115$ hours). At this point transverse shear advects fresher channel water faster than relatively salty water on the shoals. Differential advection is not important earlier in the ebb because density stratification suppresses lateral exchange between channel and shoal. During floods, transverse shear contributes little to the longitudinal dispersion of salt. Transverse baroclinic circulation during floods reduces the transverse along-channel shear, limiting longitudinal dispersion.

[42] Similar salt flux decompositions in shallow estuaries have found tidally variable longitudinal dispersivities in the Conwy [*West and Mangat*, 1986] and Tamar [*West et al.*, 1990] estuaries. In each the dispersion due to vertical shear was generally greater during stratified ebbs than during floods, consistent with our results. Dispersion due to lateral shear in these studies varied tidally, but the absolute magnitude depended on the local bathymetry. A comparison of the studies attributed greater transverse shear dispersion in the Conwy to its larger intertidal region [*West et al.*, 1990]. Intertidal zone inundation is itself a function of tidal elevation and varies with the spring/neap cycle. A larger inundation region coupled with stronger barotropic forcing made tidal pumping the dominant transport mechanism in the shallow Satilla River estuary during spring tides; during more stratified neaps baroclinic structure was most important [*Blanton et al.*, 2003]. It is likely that this tidally unsteady balance between dispersion mechanisms is relevant for any estuary with sharp density and bathymetry gradients.

6.2. Lateral Circulation and Salt Flux

[43] Transverse shear between channel and shoal disperses the longitudinal gradient and sets up lateral baroclinic circulation that is strongest during floods. As dense water moves out of the channel at the bed, return flow at the surface brings relatively fresh, lower momentum water from the shoals. This lateral flux provides a source of buoyancy that creates a stratified region during the flood immediately behind the salt front. We observe this in the field data, with relatively strong stratification after the maximum $\partial S/\partial x$ during strong floods (Figures 3b and 3c). For the remainder of the flood N^2 decreases as the destabilizing longitudinal buoyancy flux mixes away stratification. The lateral flux also injects an along-channel momentum deficit of slow moving shoal water relative to channel velocities. This reinforces the subsurface maximum in along-channel velocity during the flood (Figure 7c). Above the velocity maximum the water column is strongly stratified both because of the lateral flux of fresher shoal water and because the along-channel buoyancy flux (straining of $\partial S/\partial x$) is stabilizing. A similar case of transverse currents generating strong stratification and a subsurface velocity maximum during floods was noted in a channel in northern San Francisco Bay [*Lacy et al.*, 2003].

[44] As with the longitudinal residuals, transverse residual velocities impact the distribution of salt and other scalars. Differential advection can establish lateral circulation with opposite patterns during floods and ebbs, so we might expect net transport over the tidal cycle to be near zero. Instead, the residual velocity pattern largely reflects conditions during floods, divergent from the channel near the bed and convergent at the surface (Figure 11). Ebb/flood asymmetries deriving from the longitudinal density gradient and the intertidal elevation contribute to creating a flood-dominant pattern in the lateral residual.

[45] During ebbs the lateral flux of along channel momentum sends higher velocity water at the surface out from the channel onto the shoals, decreasing the lateral shear ($\partial U/\partial y$). The opposite is true during floods as the lateral momentum flux tends to increase lateral shear, sending relatively low velocity near-bed flow out of the channel and returning higher velocity near-surface shoal water. Enhanced lateral shear during floods reinforces differential

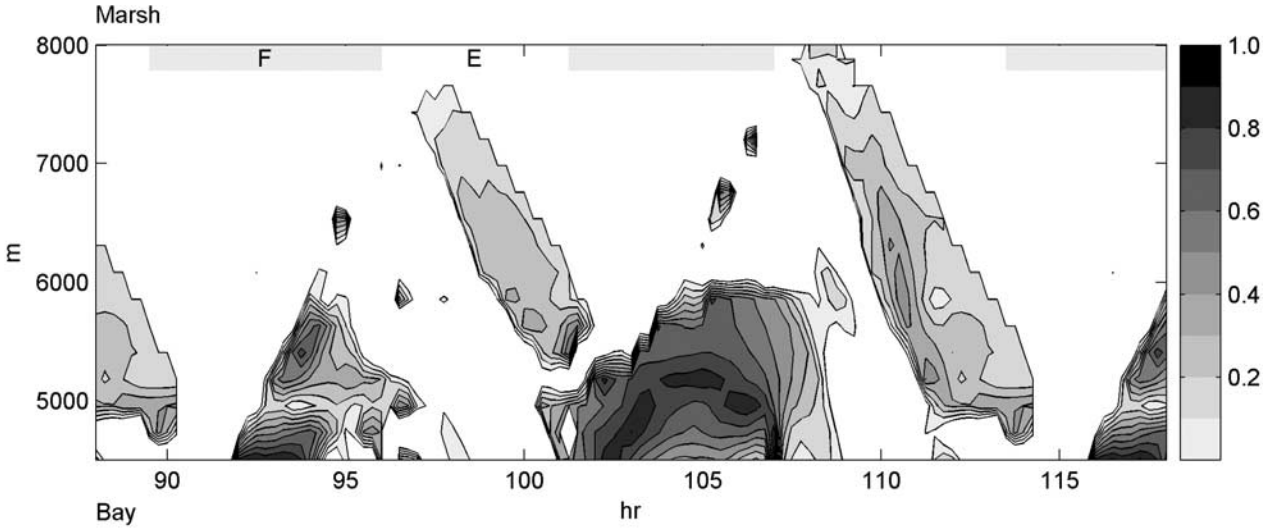

Figure 12. Lateral salt fluxes into channel from numerical model. Plotted is the fraction of total salt flux in channel due to lateral flux at channel banks: (V*S*A)/(U*S*A + V*S*A). The time series correspond with water surface and dispersivities in Figure 10.

advection of $\partial S/\partial x$, creating a stronger lateral density gradient. Consequently, the lateral baroclinic forcing and therefore the lateral circulation are stronger during floods than during ebbs [*Lerczak and Geyer*, 2004]. Another factor is that ebbs are more stratified than floods because of straining of the along-channel density gradient. Stratification during ebbs suppresses the development of transverse circulation by limiting vertical motions; floods are less stratified and the transverse circulation cells are less impeded. Thus the asymmetry in tidal straining reinforces the flood dominance of the lateral residual [*Lerczak and Geyer*, 2004].

[46] The finite inundation period of the intertidal zone impacts lateral flow asymmetry. Because $\partial S/\partial x$ resets each lower low water, the strongest longitudinal gradients are during the initial flooding of the mudflats and longitudinal dispersion decreases $\partial S/\partial x$ through the tide. Differential advection of $\partial S/\partial x$ generates lateral circulation, so for similar lateral shears the lateral density gradient is larger during floods than during ebbs. An analogous mechanism has been proposed for the flood dominance of transverse circulation in some macrotidal estuaries [*Turrell et al.*, 1996]. Finally, the large volume exchanged each tidal cycle in the intertidal zone affects the memory of the system and reinforces the ebb/flood asymmetry. Around high water slack differential advection has carried dense water farther up the channel than the shoals and lateral baroclinic exchange has the flood pattern. At the start of the ebb, flow in the channel must first unwind existing conditions before channel water is fresher than the shoals and the opposite lateral exchange pattern begins. At lower low water slack, there is no such antecedent condition because flow down the channel is diluted in the large reservoir of the bay. The strong flood begins with little memory of the previous ebb, and the flood lateral baroclinic exchange occurs for all of the rising tide. All of these factors contribute to flood dominance of the lateral residual. Residual channel/shoal exchange can be important for net transport of sediment and other scalars across the intertidal zone. For example, residual flux out of the channel at the bed could be a mechanism to move fine sediment suspended in the channel out onto mudflat shoals.

[47] If the lateral baroclinic residual is not zero, then lateral fluxes of salt into and out of the channel might impact the total salt budget. The channel is sectioned along its axis and instantaneous lateral salt flux along the channel banks ($\partial/\partial y(Avs)$) of each section is compared with the instantaneous longitudinal flux ($\partial/\partial x(Aus)$) to see when during the tidal cycle a one-dimensional salt budget might be a poor assumption (Figure 12). The fraction of the total salt flux due to lateral exchange is large only when lateral baroclinic circulation is well developed during floods behind the salinity front ($t \sim 105$ hours). Axial convergence brings low momentum shoal water into the channel, reducing the along-channel transport so the flux of water and salt in the channel is dominated by lateral advection in from the shoals. The period of significant lateral salt flux corresponds with negative values for the instantaneous K_x^V (Figure 10b). Lateral advection of relatively fresh shoal water into the channel creates a salinity deficit near the surface, and the vertical residuals of salinity and velocity combine to yield $\langle u_v s_v \rangle_A < 0$. When the model bathymetry is a flat intertidal zone with no channel, lateral baroclinic circulation does not develop. In that case the water column does not stratify behind the flood salinity front, and K_x^V does not become negative.

7. Summary and Discussion

[48] The dominant feature in the intertidal zone during periods of freshwater inflow is a distinct front between relatively fresh marsh water and saltier bay/oceanic water. In the limited span of one inundation period the salinity front disperses longitudinally, relaxing the gradient. Mechanisms for longitudinal dispersion depend on both tidal forcing and intertidal bathymetry, and the dispersivity varies substantially through the tidal cycle. As in other dispersion analyses, the mechanisms discussed here are spatial corre-

lations in velocity and salinity not explicitly resolved in the transport equation. However, the vertical and transverse structures of these correlations have very different sources and thus respond differently to changes in forcing or bathymetry.

[49] Dispersivity due to vertical structure K_x^V is strongest during stratified periods, when shearing of the velocity profile and straining of isohalines combine to expand the frontal region. Periodic stratification breaks down with increasing tidal velocities and decreasing depth, so K_x^V is most significant with relatively weak tidal forcing and in deeper flows. This combination occurs on the mudflats between lower high water and higher low water with mixed diurnal tides and could be expected to modulate through the spring/neap cycle. Vertical structure might also be important farther upstream in marsh channels, particularly in channels that are relatively deep and have low flow velocities. Turbulent mixing with breakdown of stratification vertically homogenizes the strained isohalines. Without small-scale mixing of the vertical salinity gradients the instantaneous salt fluxes during stratified ebbs would be reversed on the subsequent floods. However, even in the absence of active mixing at the end of ebbs, convective turbulence during the following flood provides mixing energy to the stratified water column.

[50] The transverse structure of velocity and salinity that create K_x^T result from bathymetric variability that could be ignored in deeper estuaries. However, shallow subtidal channels are significantly deeper than the surrounding shoals relative to the shallow flow depth. Faster, deeper flow in the channels than on the mudflats or marsh creates transverse velocity shear and differential advection of the salinity front. With stronger tidal forcing, the frictional disparity between channel and shoal is greater and K_x^T increases. The transverse structure requires exchange between channel and shoal for it to be irreversible, and lateral fluxes are enhanced by lateral baroclinic gradients due to the differential advection. Lateral exchange is relatively unimpeded on the open mudflats, but it is possible that vegetation in the marsh would restrict lateral circulation and decrease the importance of the transverse mechanism. The elevation of the shoals compared with the tidal elevation and channel bottom should also be important factors. For a very shallow channel (e.g., on the lower mudflats approaching the bay), transverse variability would be negligible; for a very deep channel (e.g., far upstream in the marsh), transverse exchange would be impeded by the channel walls for most of the tidal cycle.

[51] During the wet winter months, net transport of sediment and biological scalars, from both terrestrial and marine sources, depends on the dynamics at the tidal salinity front. Additionally, the transport of salt crucially impacts the functioning of different regions of the intertidal zone. Tidal fronts are observed in many small estuaries where inflow of dense seawater arrests outflow of buoyant riverine water [*Largier*, 1993]. Here we propose that frontal dynamics are also relevant in intertidal regions of estuaries large and small. Salinity fronts are particularly sharp in the intertidal zone because the exchange each inundation period resets conditions at lower low water. Sharp density gradients at tidal fronts impact the overall circulation and stratification and are often coincident with strong gradients in sediment and biological organisms [*Largier*, 1993]. For example, Dungeness crab larvae were observed advecting up to 10 km on a single flood tide front from the mouth of the estuary up into the intertidal zone [*Eggleston et al.*, 1998]. As the front propagated up the subtidal channels, it transitioned from a buoyant plume to an axially convergent front very much like we present here. The biological transport associated with the salinity front could be particularly important in the shallow estuarine margins that are noted for high biological productivity and act as nurseries for juvenile organisms.

[52] The negative buoyancy of sediment particles affects the net sediment transport associated with tidal fronts. Asymmetry in mixing because of periodic stratification permits greater transport of sediment upstream during relatively well mixed floods than stratified ebbs, contributing to the formation of local turbidity maxima near the upstream extent of the salinity intrusion [*Geyer*, 1993]. Enhanced bed shear stress during floods because of the combination of baroclinic circulation and tidal straining also preferentially suspends fine sediment during floods for net transport upstream [*Burchard and Baumert*, 1998]. The intertidal zone is particularly sensitive to fine sediment transport because bed elevation affects zonation of plants and organisms that in turn impact bulk flow and bed sediment properties. Flow dynamics at the salinity front likely dominate sediment transport into and out of the intertidal zone during the wet winter months.

[53] Very strong density gradients make flow and transport in the intertidal zone a three-dimensional problem. Vertical stratification in shallow flow depths and lateral variation associated with shallow subtidal channels both spring from the strong longitudinal density gradient at the tidal salinity front. Longitudinal dispersion of the salinity front relates to both the vertical and transverse structure, and the importance of each varies spatially and temporally. Along the intertidal gradient, dispersivity due to vertical structure in velocity and salinity might be expected to dominate on the lower mudflat and in the upper marsh, while transverse structure might be more important in between. Both vary on the diurnal timescale because of ebb/flood asymmetries and on the spring/neap timescale because of changes in tidal energy. Quantifying scalar fluxes in the intertidal zone is critical to our understanding of the functioning of these ecosystems.

[54] **Acknowledgments.** The authors thank Matt Brennan, Jon Fram, Maureen Martin, and Stefan Talke for assistance during the field experiment. This research was funded by National Institutes of Health grant P42ES0475 from the National Institute of Environmental Health Sciences.

References

Blanton, J. O., H. Seim, C. Alexander, J. Amft, and G. Kineke (2003), Transport of salt and suspended sediments in a curving channel of a coastal plain estuary: Satilla River, GA, *Estuarine Coastal Shelf Sci.*, *57*, 993–1006.

Bowen, M. M., and W. R. Geyer (2003), Salt transport and the time-dependent salt balance of a partially stratified estuary, *J. Geophys. Res.*, *108*(C5), 3158, doi:10.1029/2001JC001231.

Bowers, D. G., and A. Al-Barakati (1997), Tidal rectification on drying estuarine sandbanks, *Estuaries*, *20*, 559–568.

Burchard, H., and H. Baumert (1998), The formation of estuarine turbidity maxima due to density effects in the salt wedge: A hydrodynamic process study, *J. Phys. Oceanogr.*, *28*, 309–321.

Casulli, V., and E. Cattani (1994), Stability, accuracy and efficiency of a semi-implicit method for three-dimensional shallow water flow, *Comput. Math. Appl.*, *27*, 99–112.

Dronkers, J. (1996), The influence of buoyancy on transverse circulation and on estuarine dynamics, in *Buoyancy Effects on Coastal and Estuarine Dynamics*, *Coastal Estuarine Stud.*, vol. 53, pp. 341–356, AGU, Washington, D. C.

Eggleston, D. B., D. A. Armstrong, W. E. Ellis, and W. S. Patton (1998), Estuarine fronts as conduits for larval transport: Hydrodynamics and spatial distribution of Dungeness crab postlarvae, *Mar. Ecol. Prog. Ser.*, *164*, 73–82.

Fischer, H. B. (1972), Mass transport mechanisms in partially stratified estuaries, *J. Fluid Mech.*, *53*, 671–687.

Fischer, H. B., E. J. List, R. C. Y. Koh, J. Imberger, and N. H. Brooks (1979), *Mixing in Inland and Coastal Waters*, Elsevier, New York.

Galperin, B., L. H. Kantha, S. Hassid, and A. Rosati (1988), A quasi-equilibrium turbulent energy model for geophysical flows, *J. Atmos. Sci.*, *45*, 55–62.

Geyer, W. R. (1993), The importance of suppression of turbulence by stratification on the estuarine turbidity maximum, *Estuaries*, *16*, 113–125.

Geyer, W. R., J. H. Trowbridge, and M. M. Bowen (2000), The dynamics of a partially mixed estuary, *J. Phys. Oceanogr.*, *30*, 2035–2048.

Gross, E. S., V. Casulli, L. Bonaventura, and J. R. Koseff (1998), A semi-implicit method for vertical transport in multidimensional models, *Int. J. Numer. Methods Fluids*, *28*, 157–186.

Hansen, D. V., and M. Rattray Jr. (1965), Gravitational circulation in straits and estuaries, *J. Mar. Res.*, *23*, 104–122.

Lacy, J. R., M. T. Stacey, J. R. Burau, and S. G. Monismith (2003), Interaction of lateral baroclinic forcing and turbulence in an estuary, *J. Geophys. Res.*, *108*(C3), 3089, doi:10.1029/2002JC001392.

Largier, J. L. (1993), Estuarine fronts: How important are they?, *Estuaries*, *16*, 1–11.

Larsen, L. H. (1977), Dispersion of a passive contaminant in oscillatory fluid flows, *J. Phys. Oceanogr.*, *7*, 928–931.

Lerczak, J. A., and W. R. Geyer (2004), Modeling the lateral circulation in straight, stratified estuaries, *J. Phys. Oceanogr.*, *34*, 1410–1428.

Li, C., and J. O'Donnell (1997), Tidally driven residual circulation in shallow estuaries with lateral depth variation, *J. Geophys. Res.*, *102*, 27,915–27,929.

Li, C., A. Valle-Levinson, K. C. Wong, and K. M. M. Lwiza (1998), Separating baroclinic flow from tidally induced flow in estuaries, *J. Geophys. Res.*, *103*, 10,405–10,417.

MacCready, P. (1999), Estuarine adjustment to changes in river flow and tidal mixing, *J. Phys. Oceanogr.*, *29*, 708–726.

Monismith, S. G., W. Kimmerer, J. R. Burau, and M. T. Stacey (2002), Structure and flow-induced variability of the subtidal salinity field in northern San Francisco Bay, *J. Phys. Oceanogr.*, *32*, 3003–3019.

Nunes, R. A., and J. H. Simpson (1985), Axial convergence in a well-mixed estuary, *Estuarine Coastal Shelf Sci.*, *20*, 637–649.

Okubo, A. (1973), Effect of shoreline irregularities on streamwise dispersion, *Neth. J. Sea Res.*, *6*, 213–224.

Ralston, D. K., and M. T. Stacey (2005), Stratification and turbulence in subtidal channels through intertidal mudflats, *J. Geophys. Res.*, doi:10.1029/2004JC002650, in press.

Simpson, J. H., J. Brown, J. Matthews, and G. Allen (1990), Tidal straining, density, currents, and stirring in the control of estuarine stratification, *Estuaries*, *13*, 125–132.

Smith, R. (1976), Longitudinal dispersion of a buoyant contaminant in a shallow channel, *J. Fluid Mech.*, *78*, 677–688.

Smith, R. (1982), Contaminant dispersion in oscillatory flows, *J. Fluid Mech.*, *114*, 379–398.

Stacey, M. T., J. R. Burau, and S. G. Monismith (2001), Creation of residual flows in a partially stratified estuary, *J. Geophys. Res.*, *106*, 17,013–17,037.

Turrell, W. R., J. Brown, and J. H. Simpson (1996), Salt intrusion and secondary flow in a shallow, well-mixed estuary, *Estuarine Coastal Shelf Sci.*, *42*, 153–169.

West, J. R., and J. S. Mangat (1986), The determination and prediction of longitudinal dispersion coefficients in a narrow, shallow estuary, *Estuarine Coastal Shelf Sci.*, *22*, 161–181.

West, J. R., R. J. Uncles, J. A. Stephens, and K. Shiono (1990), Longitudinal dispersion processes in the upper Tamar estuary, *Estuaries*, *13*, 118–124.

Wong, K. C. (1994), On the nature of transverse variability in a coastal plain estuary, *J. Geophys. Res.*, *99*, 14,209–14,222.

Yasuda, H. (1984), Longitudinal dispersion of matter due to the shear effect of steady and oscillatory currents, *J. Fluid Mech.*, *148*, 383–403.

D. K. Ralston and M. T. Stacey, Department of Civil and Environmental Engineering, University of California, Berkeley, Berkeley, CA 94720, USA. (dralston@berkeley.edu)